ACS APPLIED MATERIALS & INTERFACES

Research Article

www.acsami.org

Open Access on 07/15/2015

Size-Tunable and Monodisperse Tm^{3+}/Gd^{3+}-Doped Hexagonal $NaYbF_4$ Nanoparticles with Engineered Efficient Near Infrared-to-Near Infrared Upconversion for In Vivo Imaging

Jossana A. Damasco,[†] Guanying Chen,*[,†,‡] Wei Shao,[†,‡] Hans Ågren,[§] Haoyuan Huang,[∥] Wentao Song,[∥] Jonathan F. Lovell,[∥] and Paras N. Prasad*[,†,⊥]

[†]Department of Chemistry and Institute for Lasers, Photonics, and Biophotonics, University at Buffalo, The State University of New York, Buffalo, New York 14260-3000, United States

[‡]School of Chemical Engineering and Technology, Harbin Institute of Technology, Harbin, Heilongjiang 150001, China

[§]Department of Theoretical Chemistry and Biology, School of Biotechnology, Royal Institute of Technology, SE-10691 Stockholm, Sweden

[∥]Department of Biomedical Engineering, University at Buffalo, The State University of New York, Buffalo, New York 14260-3000, United States

[⊥]Department of Chemistry, Korea University, Seoul 136-701, Korea

Supporting Information

ABSTRACT: Hexagonal $NaYbF_4:Tm^{3+}$ upconversion nanoparticles hold promise for use in high contrast near-infrared-to-near-infrared (NIR-to-NIR) in vitro and in vivo bioimaging. However, significant hurdles remain in their preparation and control of their morphology and size, as well as in enhancement of their upconversion efficiency. Here, we describe a systematic approach to produce highly controlled hexagonal $NaYbF_4:Tm^{3+}$ nanoparticles with superior upconversion. We found that doping appropriate concentrations of trivalent gadolinium (Gd^{3+}) can convert $NaYbF_4:Tm^{3+}$ 0.5% nanoparticles with cubic phase and irregular shape into highly monodisperse $NaYbF_4:Tm^{3+}$ 0.5% nanoplates or nanospheres in a pure hexagonal-phase and of tunable size. The intensity and the lifetime of the upconverted NIR luminescence at 800 nm exhibit a direct dependence on the size distribution of the resulting nanoparticles, being ascribed to the varied surface-to-volume ratios determined by the different nanoparticle size. Epitaxial growth of a thin $NaYF_4$ shell layer of ~2 nm on the ~22 nm core of hexagonal $NaYbF_4:Gd^{3+}$ 30%/Tm^{3+} 0.5% nanoparticles resulted in a dramatic 350 fold NIR upconversion efficiency enhancement, because of effective suppression of surface-related quenching mechanisms. In vivo NIR-to-NIR upconversion imaging was demonstrated using a dispersion of phospholipid-polyethylene glycol (DSPE-PEG)-coated core/shell nanoparticles in phosphate buffered saline.

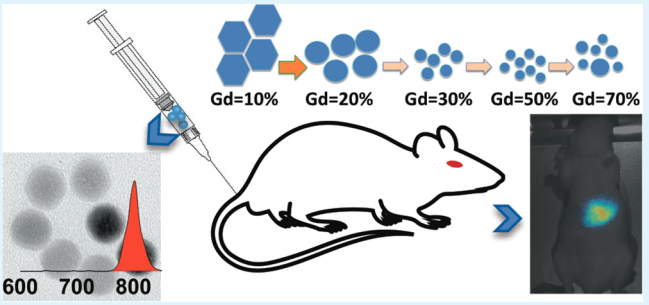

KEYWORDS: *near-infrared, upconversion nanocrystals, core−shell, bioimaging*

INTRODUCTION

Lanthanide-doped upconversion nanoparticles (UCNPs), usually utilizing near-infrared (NIR) excitation, while emitting in a shorter wavelength NIR, or visible range, are receiving a great deal of attention for potential application in bioimaging. This is due to the numerous advantages associated with NIR excitation, such as the absence of any autofluorescence background noise, deep penetration of NIR excitation light into biological tissue, no photobleaching, no blinking, and reduced photodamage. In addition, they exhibit low toxicity.[1−9] These merits are essentially empowered by the unique optical attributes of UC, which delineates emission of higher energy photon through a series of linear absorption of lower energy photons or ion-to-ion energy transfers in lanthanides.[10] In essence, UC utilizes real, long-lived intermediate energy states of trivalent lanthanide ions to store and transfer energy. This yields highly efficient upconverted emission under continuous-wave (CW) excitation condition in contrast to conventional multiphoton-absorption-induced fluorescence, which involves virtual intermediate energy states. Therefore, UC emission is achievable by using a low-cost CW laser diode, thus eliminating the need of an expensive high peak power pulsed laser excitation as required in conventional multiphoton experiments.[7,10,11] These myriad eminent advantages of UCNPs lead them to be a promising new class of optical biolabels.

Received: May 26, 2014
Accepted: July 15, 2014
Published: July 15, 2014

Among lanthanide-doped UCNPs, NIR-to-NIR Yb^{3+}/Tm^{3+}-codoped $NaYF_4$ nanoparticles are of particular interest. Not only is the $NaYF_4$ (either cubic or hexagonal phase) proven to be one of the most efficient host materials for UCNPs, the Yb^{3+}/Tm^{3+} dopants allow the excitation at around 975 nm with the photoluminescence (PL) emission peak at 800 nm, both within the spectral range of 750−1000 considered as the "window of optical transparency" for biological tissues.[12,13] This feature allows high contrast in vitro and in vivo optical bioimaging, as both light attenuation and scattering are significantly reduced in the NIR spectral range and the autofluorescence of cells and tissues is absent under the conditions of UC excitation and emission. Recently, we have demonstrated that similar size cubic $NaYbF_4:Tm^{3+}$ nanoparticles are much more efficient than the typically used cubic $NaYF_4$ nanoparticles doped with 20−30 mol % Yb^{3+} and 0.5−1% Tm^{3+} ions. Higher Yb^{3+} concentration has resulted in an increased absorption cross-section per nanoparticle and enhanced energy transfer rates between Yb^{3+} and Tm^{3+} ions. This feature makes cubic $NaYbF_4:Tm^{3+}$ nanoparticles more attractive for pertinent bioapplications.[12] Moreover, by coating them with a biocompatible CaF_2 shell, their NIR UC PL was enhanced by about 35 times, providing high efficiency to entail high contrast deep tissue bioimaging.[13,14] Nevertheless, the achieved results are demonstrated in the $NaYbF_4:Tm^{3+}$ nanoparticles of a cubic phase. It is known that the hexagonal phase $NaYF_4$ host lattice is about 10-fold more efficient than the cubic phase $NaYF_4$.[15,16] This is because the hexagonal phase $NaYF_4$ has a lower C_1 site symmetry than the O_h site symmetry of the cubic phase for lanthanide ions, and that it also has a shorter distance of 3.548 Å than 3.868 Å of the cubic form between two adjacent lanthanide ion neighbors, thus favoring higher UC efficiency. As a consequence, it will be of great interest to advance the hexagonal phase $NaYbF_4:Tm^{3+}$ nanoparticles in the preparation, the luminescence efficiency enhancement, as well as in high contrast bioimaging. However, to our knowledge this has not yet been reported.

While the hexagonal $NaYF_4$ nanoparticles doped with lower Yb^{3+} concentrations of 20−30% and activator ions (Tm^{3+}, Er^{3+}, or Ho^{3+}) of 0.5−2% have been successfully synthesized using various chemical methods, it is nontrivial to prepare small size Tm^{3+}-doped hexagonal $NaYbF_4$ nanoparticles due to its distinct growth dynamics from the hexagonal $NaYF_4$ nanoparticles.[17] The typically used Ostwald-ripening methods or thermolysis procedures for synthesizing uniform hexagonal lanthanide-doped $NaYF_4$ nanoparticles generally result in lanthanide-doped $NaYbF_4$ nanoparticles of cubic form[12,13,18−20] or hexagonal $NaYbF_4$ plates with the size of 152 × 93 nm.[21] Hydrothermal or solvothermal approaches often result in cubic $NaYbF_4$ microtubes[22] or uniform nanoplates of cubic form,[23] rarely producing small size hexagonal $NaYbF_4$ nanoparticles.[24] Until this point, limited success has been met in the preparation of highly efficient NIR-to-NIR converting hexagonal $NaYbF_4:Tm^{3+}$ nanoparticles. It has been recently realized that doping of trivalent gadolinium (Gd^{3+}) can significantly alter the fundamental nucleation and growth processes of the $NaYF_4$ nanoparticles during hydrothermal synthesis, providing an efficient way to tune their size and phase.[25] Doping of other lanthanide ions into SrF_2 during a hydrothermal process[26] or into CeO_2 nanoparticles during a thermolysis process[27] can also modify the size and the phase of resulting nanoparticles due to the generation of transient electric dipoles in growing nanoparticles. The Ostwald-Ripening method is a well-established procedure to produce highly uniform hexagonal $NaYF_4$ upconversion nanoparticles, but has not yet met success in producing small size hexagonal $NaYbF_4:Tm^{3+}$ nanoparticles. Moreover, because the $NaYbF_4:Tm^{3+}$ nanoparticles contain a large amount of Yb^{3+} ions in the lattice, Yb^{3+}-mediated energy transfers of excited energy to surface lanthanide ions or surface deactivation sites will be extremely high. This seriously limits the UC efficiency of this type of nanoparticles as well as their ability to be used as imaging contrast agents.

Herein, we present the preparation of uniform hexagonal $NaYbF_4:Tm^{3+}$ nanoparticles using the Ostwald-Ripening method and doping Gd^{3+} at precisely defined concentrations to achieve a tunable size. The UC PL intensities and lifetimes of the resulting nanoparticles were studied and analyzed in relation to the size and the phase of these nanoparticles. A thin layer of ∼2 nm inert $NaYF_4$ matrix was grown as a shell on top of the hexagonal core $NaYbF_4:Gd^{3+}/Tm^{3+}$ UCNPs (∼22 nm) to minimize surface-related quenching mechanisms. This yields a dramatic enhancement of about ∼350 folds in NIR UC PL at ∼800 nm. To demonstrate their ability for high contrast imaging in vivo, NIR-to-NIR UC PL imaging of a nude mouse were performed using phospholipid-polyethylene glycol (DSPE-PEG)-coated core/shell $(NaYbF_4:Gd^{3+}/Tm^{3+})/NaYF_4$ nanoparticles dispersed in phosphate buffered saline.

RESULTS AND DISCUSSION

Characterization of the Resulting $NaYb_{(1-x)}Gd_{(x)}F_4:Tm^{3+}$ 0.5% Nanoparticles. The crystallinity and phase transformation of the synthesized nanoparticles with varying Gd^{3+} dopant concentrations were determined by the XRD patterns (Figure 1). All synthesized nanoparticles show well-defined peaks, confirming their good crystallinity. The XRD pattern in Figure 1a agrees well with the standard cubic $NaYbF_4$ pattern of JCPDS 77-2043, indicating a pure cubic phase structure for the undoped $NaYbF_4$. The beginning of the cubic-to-hexagonal phase transformation is detectable by XRD for Gd^{3+} doping concentration of 7%, as can be seen in Figure 1b. An enlarged XRD pattern of Figure 1b is shown in

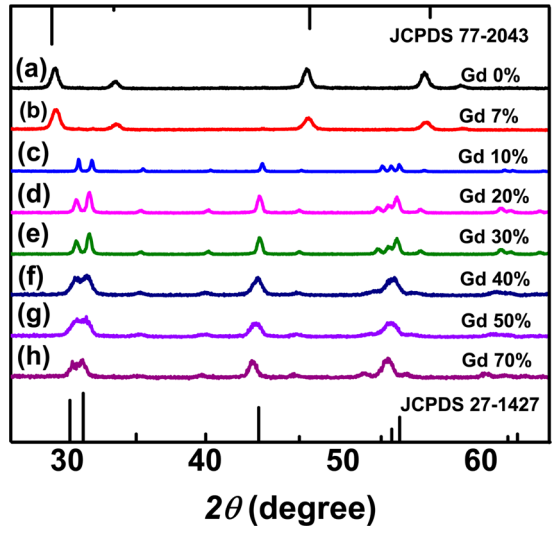

Figure 1. XRD patterns of $NaYb_{(1-x)}Gd_{(x)}F_4$: Tm^{3+} 0.5% with (a) x = 0, (b) x = 0.07, (c) x = 0.1, (d) x = 0.2, (e) x = 0.3, (f) x = 0.4, (g) x = 0.5, (h) x = 0.7 with standard diffraction patterns for the alpha (JCPDS 77-2043) and beta (JCPDS 27-1427) phases of $NaYbF_4$.

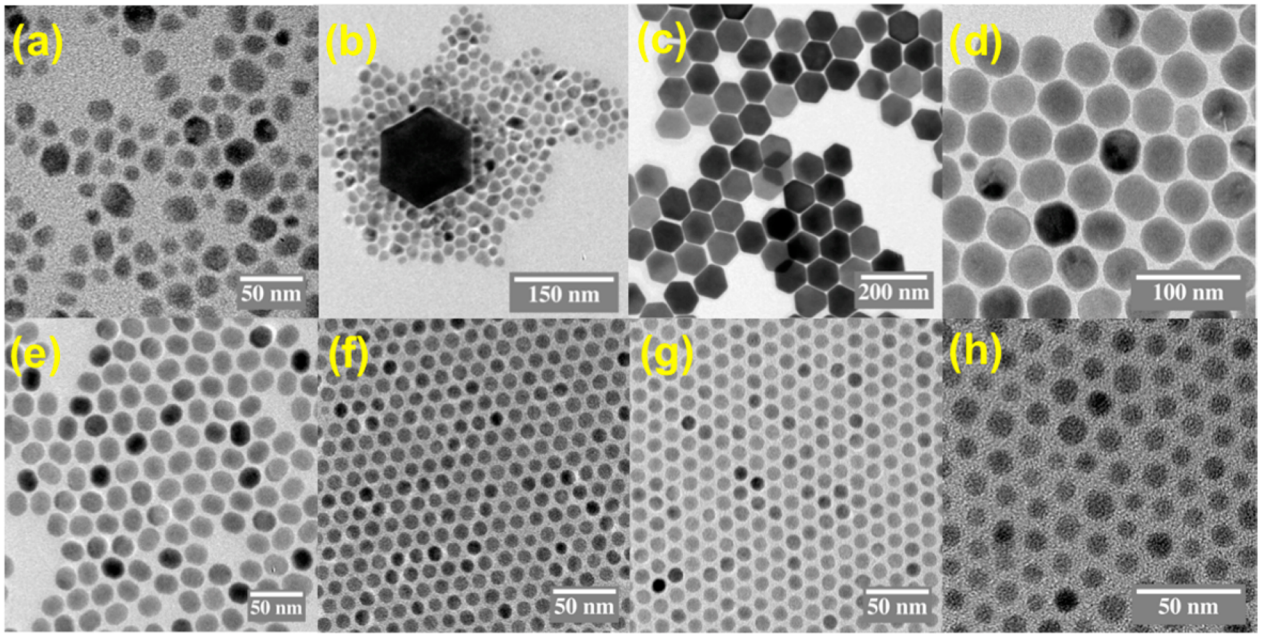

Figure 2. TEM images of $NaYb_{(1-x)}Gd_{(x)}F_4$: Tm^{3+} 0.5% with (a) $x = 0$, (b) $x = 0.07$, (c) $x = 0.1$, (d) $x = 0.2$, (e) $x = 0.3$, (f) $x = 0.4$, (g) $x = 0.5$, (h) $x = 0.7$.

Supporting Information, Figure S2A. To investigate this phase transformation further, we also prepared $NaYbF_4$ doped with Gd^{3+} of 5% (Supporting Information, Figure S1). Although the XRD pattern of Gd^{3+} 5% (Supporting Information, Figure S1A) shows no detectable peaks of the hexagonal phase, small amounts of large particles of 90 nm size were observed among the predominantly small nanoparticles with average sizes below 20 nm (Supporting Information, Figure S1B). The TEM results for nanoparticles doped with Gd^{3+} of 5% are quite similar to that of the nanoparticles doped with 7% Gd^{3+}. This similarity suggests that the phase transformation began to take place at 5% Gd^{3+}, but only became detectable by XRD at 7% Gd^{3+}. Figure 1c–f indicates that substitution of more than 10% Yb^{3+} with larger Gd^{3+} ions can result in a complete formation of purely β-phase nanoparticles, with XRD patterns in agreement with the standard pattern of JCPDS 27-1427 of β-phase $NaYbF_4$. However, the widths of XRD peaks, for example, the main peak at ~30°, vary with the Gd^{3+} concentration, indicating a change in the resulting particle size. It is known that the size and the width of a diffraction peak can be correlated by the Scherrer's equation[12]

$$D = K\lambda/\beta \cos\theta \quad (1)$$

where $K = 0.89$, D represents the crystallite size (in nanometers), λ is the wavelength of the Cu Kα radiation, β is the corrected half-width of the main diffraction peak, and θ is the Bragg's angle of diffraction peak. According to eq 1, a gradual broadening of the XRD peaks in Figure 1c–h indicates a decrease in size of the formed nanoparticles as the Gd^{3+} ion concentration is increased. The average nanoparticle sizes were calculated to be 80, 44, 20, and 10 nm for Gd^{3+} of 10, 20, 30, and 40%, respectively. The nearly identical XRD peak widths in Figures f and g indicate a similar particle size for nanoparticles doped with a Gd^{3+} concentration of 40–50%, while a slight narrowing of the peaks for Gd 70% compared to that of Gd 40–50% indicates a slight increase in the average nanoparticle size. These conclusions are in general agreement with the TEM results shown in Figure 2.

Figure 2a–h shows the TEM results for $NaYbF_4$ particles doped with Tm^{3+} of 0.5% and various Gd^{3+} concentrations of 0%, 7%, 10%, 20%, 30%, 40%, 50%, and 70%, respectively. It can be observed that the introduction of Gd^{3+} ions to the $NaYbF_4$ matrix can facilitate the formation of uniform nanoparticles and induce a significant decrease in the size of the nanoparticles. The $NaYbF_4$:Tm^{3+} particles produced with 10% or less Gd-doping are irregular particles of varying sizes, while substitution of 10% Yb^{3+} with Gd^{3+} ions yielded uniform nanoparticles with an average diameter of around 100 nm. An inverse relationship between the amount of Gd^{3+} ions and the resulting size of the nanoparticles was shown for Gd^{3+} between 10 and 40%. The smallest particle diameter with uniform distribution averaged at 12 nm which was achieved by substituting 40—50% Gd^{3+} ions. Increasing the amount of Gd^{3+} to 70% results in the formation of a divergent size distribution, varying from 7 to 15 nm or larger. These observations are consistent with the results of the XRD in Figure 1. The dependence of the average particle size on the Gd^{3+} concentration is clearly shown in Figure 3. It is worth noting that the occurrence of phase transformation as shown in Figure 1 is clearly associated with a size disorder at Gd^{3+} concentration of 5–7%, and the resulting pure hexagonal phase $NaYbF_4$ doped with Gd^{3+} of 10% is much larger than the size of cubic phase $NaYbF_4$ without any Gd^{3+} doping.

Mechanisms for Phase and Size Tuning of the Resulting $NaYb_{(1-x)}Gd_{(x)}F_4$: Tm^{3+} 0.5% Nanoparticles. The formation of the β-phase (hexagonal phase) nanoparticles in this experiment is believed to arise from a lowering of the energy barrier for the $\alpha \rightarrow \beta$ (cubic to hexagonal) phase transition due to doping of the larger lanthanide ions. It is well established that the α-phase is a metastable phase, while the β phase is a thermodynamically stable phase. However, α-$NaREF_4$ is favored to form during the particle growth because of the high surface energy produced by the nanosize effect. The formation of the hexagonal phase would require a higher thermal energy compared to the cubic phase, if all the remaining conditions are kept constant. This is generally

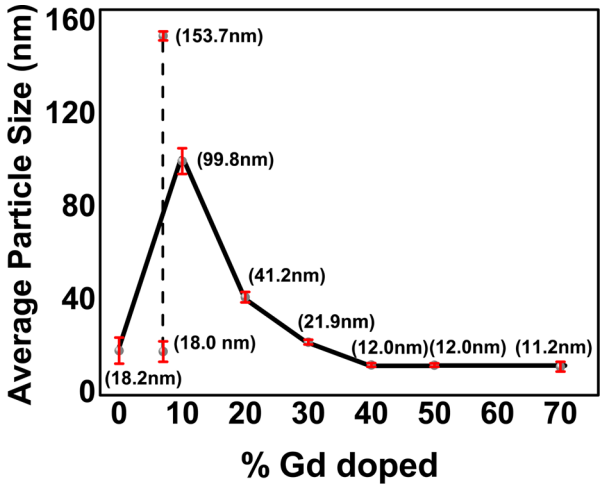

Figure 3. Average diameter of particle versus the corresponding Gd^{3+} doping concentration. The dashed vertical line at Gd^{3+} of 7% connects the two particle-size distributions resulting from nanoparticles of a mixed cubic and hexagonal phase.

because of the existence of an energy barrier for the $\alpha \rightarrow \beta$ phase transition. Fundamentally, the cubic-to-hexagonal phase transition involves a disorder-to-order character change of the cations in the host lattice.[28] The Na^+ and RE^{3+} ions are randomly distributed in the cationic sublattice of the cubic structure, whereas there are three types of cation sites in the hexagonal structure.[21,29] Hence, the structural change because of the phase transformation will need a significant electron cloud distortion.[30] Light lanthanides have larger radius and, thus, are more polarizable and more favorable for electron cloud distortion. Doping of light lanthanides into the host lattice can therefore result in lowering of the energy barrier for the phase transition. For this reason, the addition of 10% Gd^{3+} ions resulted in energy barrier low enough to be overcome at a lower temperature within a short reaction time (300 °C, 1.5 h) to achieve a complete $\alpha \rightarrow \beta$ transition.

Smaller nanoparticles are obtained when the added Gd^{3+} ions are greater than 10%. Density functional theory (DFT) calculations performed by Liu and co-workers[30] have shown that substitution of Gd^{3+} to Y^{3+} ions resulted in surface modification that has increased the surface charge density of the $NaYF_4$ crystal surface. This increase in electron charge density retarded the diffusion of the needed fluoride anion to the crystal surface due to charge repulsion. The same principle applied to the size tuning of $NaYbF_4$ here. The Gd^{3+} ions have a larger radius (r = 93.5 pm) leading to a less electropositive surface in comparison with the smaller Yb^{3+} ion (r = 86.8 pm).[31] Increasing the Gd^{3+} content to 40−50% decreased the rate of diffusion of F^- ions significantly, slowing the formation of the crystal nuclei. Thus, under identical conditions, a decrease in the diffusion rate of the F^- ions resulting in smaller nuclei limits the particle growth; hence, smaller sized nanoparticles are formed. Further increase of Gd^{3+} content to 70% shows a mixture of smaller particles (7−10 nm) and considerably larger particles ~15 nm. The efficient retardation of fluoride diffusion at this high Gd^{3+} concentration can result in the formation of nanoparticles with size smaller than a critical size. These nanoparticles are unstable because of their high surface energy, and thus can be dissolved or aggregated in favor of the growth of larger crystals. From this picture, one can infer that this typical Ostwald ripening process caused the diverging of particle sizes at Gd^{3+} 70%.

UC PL Spectra of $NaYb_{(1-x)}Gd_{(x)}F_4:Tm^{3+}$ 0.5% Nanoparticles. The UC PL were measured for $NaYb_{(1-x)}Gd_{(x)}F_4:Tm^{3+}$ 0.5% nanoparticles of varying sizes dispersed in hexane. To allow for accurate comparison, the concentration of each nanoparticle solution and all the pertinent parameters for UC PL measurement were kept the same. Figure 5a shows the UC PL spectra under 975 nm laser diode excitation of the synthesized $NaYb_{(1-x)}Gd_{(x)}F_4$: Tm^{3+} 0.5% nanoparticles in a hexane suspension. There are six resolved UC PL bands corresponding to Tm^{3+} transitions. The strongest peak appears at 801 nm, corresponding to the $^3H_4 \rightarrow {}^3H_6$ transition. The peak at 700 nm corresponds to $^3F_{2,3} \rightarrow {}^3H_6$. The four weak ones are shown in the inset with maxima at 358, 450, 471, and 650 nm matching the transitions $^1I_6 \rightarrow {}^3F_4$, $^1D_2 \rightarrow {}^3F_4$, $^1G_4 \rightarrow {}^3H_6$, and $^1G_4 \rightarrow {}^3F_4$, respectively. It is striking that the NIR UC PL band peaked at 801 nm is significantly more intense than all the other UC PL bands, making these nanoparticles highly suitable for bioimaging.

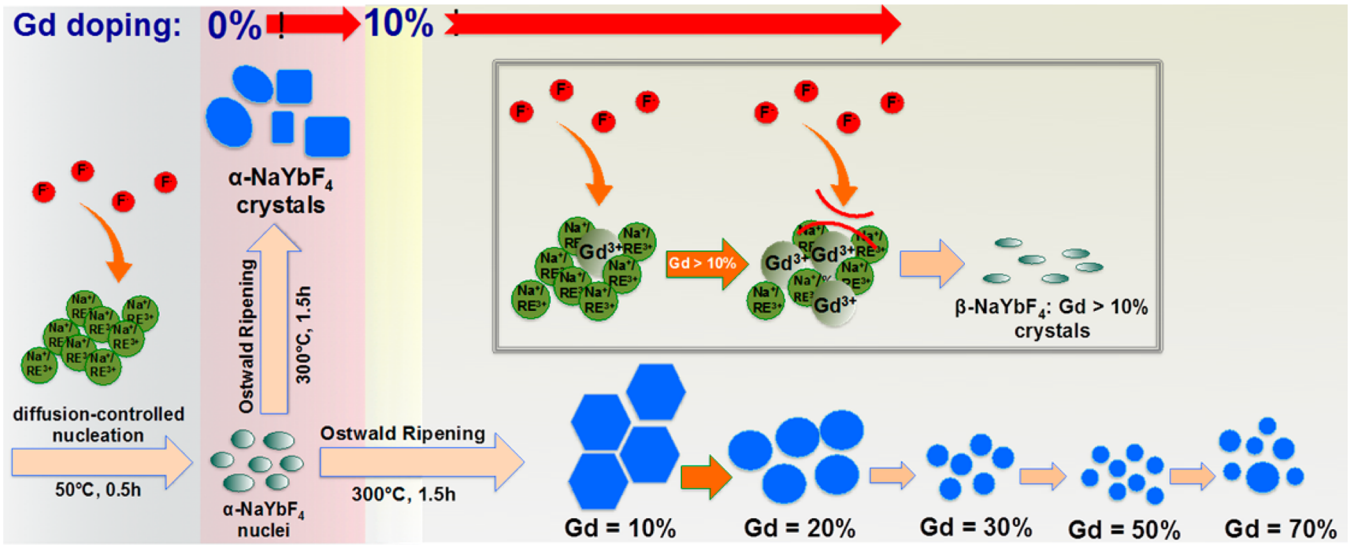

Figure 4. Schematic illustration of the phase transition and size reduction through lanthanide doping.

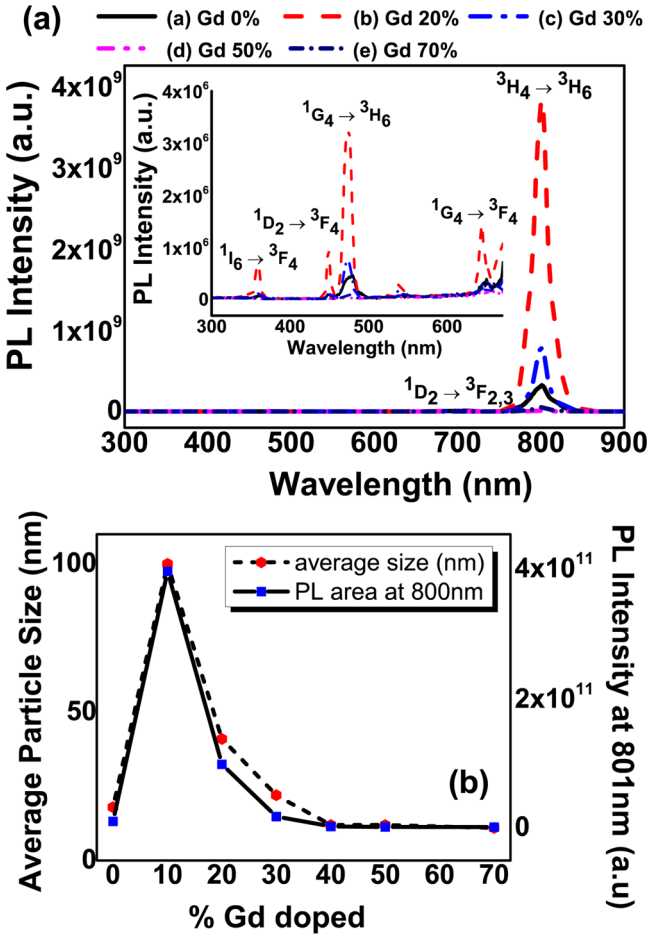

Figure 5. (a) UC PL Spectra of $NaYb_{(1-x)}Gd_{(x)}F_4$: Tm^{3+} 0.5% (a) x = 0%, (b) x = 20%, (c) x = 30%, (d) x = 50%, and (e) x = 70%. The inset shows an enlarged vision of the weak UV and visible peaks in the range of 300−650 nm. (b) Plot of the PL intensities at 801 nm of $NaYb_{(1-x)}Gd_{(x)}F_4$: Tm^{3+} 0.5% (x = 0%, 10%, 20%, 30%, 40%, 50%, 70%) and the average particle size, both with respect to the Gd concentrations.

A comparison of the intensities of emission at 801 nm (Figure 5b) shows that the intensity is increased by about 40 times with the addition of 10% Gd^{3+} ions, when compared to that of the pure cubic $NaYbF_4$ nanoparticles. Two factors can contribute to this increase. The first factor is the increase in size. The cubic $NaYbF_4$ nanoparticles have a mixture of size from 10 to 30 nm, while the $NaGd_{0.2}Yb_{0.8}F_4$ nanoparticles have an average diameter of 100 nm. Larger nanoparticles have lower surface quenching centers due to a smaller surface-to-volume ratio, thus exhibiting a higher PL intensity. The second factor is the phase transition from the cubic $NaYbF_4$ host lattice to the pure hexagonal $NaGd_{0.2}Yb_{0.8}F_4$. Hexagonal-phase nanoparticles are known to be more efficient than their cubic-phase counterparts.[32,33] However, a similar dependence of PL, as well as the nanoparticle size on the Gd^{3+} concentration, as shown in Figure 5b, demonstrates the dominant role of the size factor for PL increase. A monotonous decrease of PL intensity is observed for Gd^{3+} concentration over 10%. Increasing the amount of Gd^{3+} to 50% and 70% diminishes the intensities to be 3% and 16% of the UC PL intensity of hexagonal $NaGd_{0.2}Yb_{0.8}F_4$:Tm^{3+} 0.5% nanoparticles. This decrease in the UC PL intensity is due to a decrease in the particle size as well as due to the decrease of the sensitizer concentration of Yb^{3+} ions. However, time-resolved PL spectra shown in Figure 6 suggest that the size-dependent surface-related quenching effect

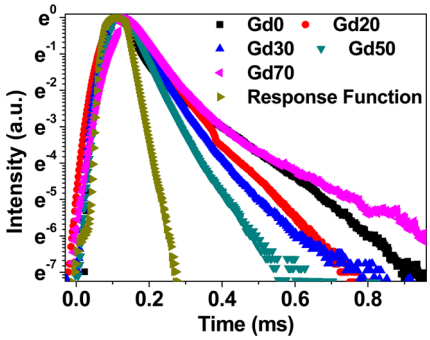

Figure 6. PL decays at 801 nm of $NaYb_{(1-x)}Gd_{(x)}F_4$: Tm^{3+} 0.5% (x = 0%, 20%, 30%, 50%, 70%) nanoparticles.

plays an important role in lowering the UC PL intensity. This conclusion can also be suggested by a linear dependence of the UC PL intensity on the nanoparticle surface area (Supporting Information, Figure S4)

PL Lifetimes of $NaYb_{(1-x)}Gd_{(x)}F_4$: Tm^{3+} 0.5% Nanoparticles. Figure 6 displays a semilogarithmic plot of PL decay at 801 nm for the $NaYb_{(1-x)}Gd_{(x)}F_4$: Tm^{3+} 0.5% (x = 0%, 20%, 30%, 50%, 70%) nanoparticles. Because of similar PL decay profiles for Gd^{3+} ions of 40% and 50%, the PL decay for the Gd^{3+} ions of 40% is intentionally omitted in Figure 6 for clarity. The lifetime of the PL at 801 nm of these nanoparticles can be expressed in general as follows:[34]

$$\frac{1}{\tau} = \frac{1}{\tau_0} + K[Q] = \frac{1}{\tau_0} + W\left[\frac{SA}{V}\right] \quad (2)$$

where τ is the observed lifetime of the $^3H_4$ state, τ_0 is the natural lifetime of the $^3H_4$ state, K is a constant related to surface quenching, $[Q]$ is the surface quenching rate, W is a modified constant related to the surface quenching, $[SA/V]$ is the surface to volume ratio of the nanoparticles. The hypothesis here in eq 2 is a linear relationship between the surface quenching rate and the surface-to-volume ratio, SA/V. This is reasonable, as a higher surface-to-volume ratio will expose more lanthanide ions on the surface to the surrounding quenchers. According to eq 2, it can be concluded that nanoparticles of different sizes will have varied lifetimes, and a broad size distribution of nanoparticles will lead to serious deviations from a linear relation in a semilogarithmic plot of PL decay. Indeed, the semilogarithmic plots of PL decays at 801 nm for Gd^{3+} 0% and for Gd^{3+} 70% nanoparticles have nonlinear dependences, owing to a broad size distribution as seen in Figure 2a and h. Since Gd^{3+} doping between 20 and 50% has resulted in very uniform size distributions of nanoparticles, the PL decays for these samples can be roughly linear. We also tried to use biexponential functions to fit the PL decay plots of Gd^{3+} 20−50%, which show slight bending of the curve. However, the result ended up with two identical exponential functions for the best fitting. The slight deviation of decays of Gd^{3+} 20−50% from a linear function in Figure 6 might be due to ion−ion interactions that produce nonradiative decay pathways for the $^3H_4$ state, and the different environment of lanthanide ions inside the nanoparticle or on the particle surface. The doping of Gd^{3+} 20, 30, and 50% has led the size of hexagonal nanoparticles to become 41, 22, and 12 nm, respectively.

dx.doi.org/10.1021/am503288d | ACS Appl. Mater. Interfaces 2014, 6, 13884−13893

This size reduction correlates with a corresponding reduction in the average lifetime, from 87.8 to 65.7 and to 55.9 μs, respectively. Indeed, the inverse of the lifetime exhibits a clearly linear dependence on the surface to volume ratio of these nanoparticles (Supporting Information, Figure S6), as suggested by eq 2.

Core−Shell Structure of $NaYbF_4$: Gd^{3+}30%, Tm^{3+} 0.5% @$NaYF_4$ Nanoparticles. The result in Figure 6 has clearly indicated that surface-related quenching effects play an important role in limiting the UC PL intensity. Surface-related deactivations may occur in two ways: (i) photoexcited dopants located on or around the surface can be deactivated directly by neighboring quenching centers (such as ligand passivation, solvents, surface impurities, surface lattice defects); (ii) the energy contained in the photoexcited dopants located in the center of nanoparticles can randomly migrate and travel a long distance to the dopant on/around surface or directly to the surface quenching sites. In particular, due to the unique two-energy-level structure of Yb^{3+} in association with its long-lived excited state, a long distance transportation of energy in the Yb^{3+} sublattice is highly efficient in $NaYbF_4$-based UC materials. As a consequence, the potential of UC PL intensity in lanthanide-doped $NaYbF_4$ is severely limited by surface-related quenching. A useful strategy to address this problem is to use a core−shell architecture, in which the epitaxial shell not only isolate lanthanide dopants from the environment but can also passivate surface lattice defects. As a result, the two possible quenching ways by surface-related deactivation can be simultaneously suppressed by a core/shell structure.[35,36]

Here, we selected $NaYbF_4$:Tm^{3+} 0.5% nanoparticle doped with Gd^{3+} 30% to further build up a core/shell nanoparticles, since it has a relatively small size, but still contains a large amount of Yb^{3+} ions that can be engineered to produce favorable UC PL. Figure 7 shows (a) the size distribution, (b) TEM images at lower magnification, and (c) high resolution TEM (HRTEM) of the resulting ($NaYbF_4$:Gd^{3+}30%, Tm^{3+}0.5%)@$NaYF_4$ core−shell nanoparticles. As shown in Figure 7a and b, the resulting core−shell particles were uniform, with an average diameter of 25.22 ± 1.05 nm, which is larger than the average core size of ~21.9 nm, as displayed in Figure 3. The size difference between the core and the core/shell nanoparticles suggest a successful epitaxial growth of a thin $NaYF_4$ layer of ~2 nm. To confirm the formulation of the core/shell structure, HRTEM was utilized to image a single core/shell nanoparticle. As one can see in Figure 7c, a clear core/shell structure is seen with a discernible contrast between the core (dark) and the shell (light). This contrast is produced by the different electron scattering capability between the core and the shell due to a large difference in the atomic number between the Yb^{3+} (in the $NaYbF_4$ host lattice) at the core and the Y^{3+} (in the $NaYF_4$ host lattice) at the shell. Moreover, the shell thickness is determined to be about ~3 nm for this single nanoparticle, in general accordance with the average thickness of ~2 nm estimated by the size difference between the core and the core/shell nanoparticles. The formation of a core/shell structure is also supported by the appearance of Y^{3+} element peak in the energy dispersive spectroscopy of these core/shell nanoparticles (Supporting Information, Figure S7).

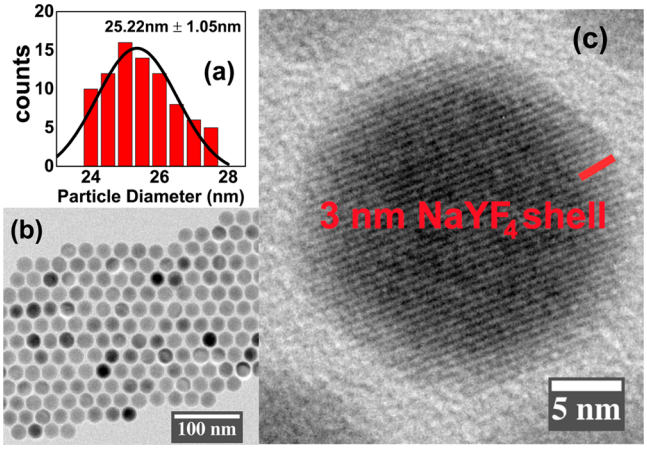

Figure 7. (a) Size distribution, (b) TEM image, and (c) HRTEM of the $NaYbF_4$: Gd^{3+} 30%, Tm^{3+} 0.5%@$NaYF_4$ core−shell nanoparticles.

The UC PL of the core and the core/shell nanoparticles dispersed in hexane were compared and shown in Figure 8. As the UC PL from the core nanoparticles is hard to see, a zooming-in is shown in the inset of Figure 8. As one can see, the NIR UC PL at 800 nm in the core/shell nanoparticles is about 350 times higher than that of the core nanoparticles. This result provides compelling evidence that the ~2 nm inert $NaYF_4$ shell has effectively suppressed surface-related quenching mechanisms. This conclusion is further supported by the observation of a prolonged lifetime of UC PL at 800 nm in the core/shell nanoparticles than in the core nanoparticles (Supporting Information, Figure S8). Moreover, we also compared the UC PL of the 25 nm core−shell ($NaYbF_4$:Tm 0.5%, Gd^{3+} 30%)/$NaYF_4$ with that of the ~100 nm sized hexagonal $NaYbF_4$:Tm^{3+} 0.5%, Gd^{3+} 10% (Supporting Information, Figure S9). Although having a significantly smaller particle size and lower Yb^{3+} sensitizer concentration, the core/shell nanoparticles is still 10 times more efficient than the ~100 nm sized hexagonal $NaYbF_4$:Tm^{3+} 0.5%, Gd^{3+} 10% UCNPs, clearly showing the merit of the core/shell structure to suppress surface-related quenching. Moreover, the enhanced UC PL in the core/shell nanoparticles is appealing for bioimaging, as a lower dose of them will be needed to administer into the bodies

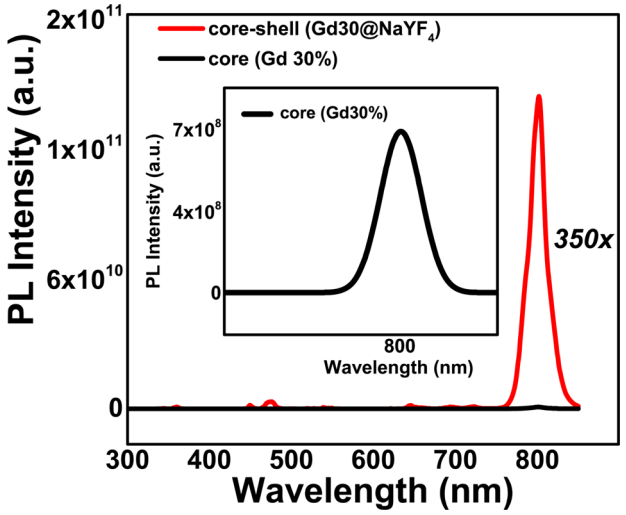

Figure 8. Compared PL intensity of the core/shell $NaYbF_4$: Gd^{3+} 30%, Tm^{3+} 0.5%@$NaYF_4$ nanoparticles with that of the core $NaYbF_4$: Gd^{3+} 30%, Tm^{3+} 0.5% nanoparticles. The inset shows an enlarged view of the PL from the core $NaYbF_4$: Gd^{3+} 30%, Tm^{3+} 0.5% nanoparticles.

to perform the imaging modality, therefore reducing any potential harmful effects.

In Vivo Imaging Using Core−Shell ($NaYbF_4$:Tm^{3+} 0.5%, Gd^{3+} 30%)/$NaYF_4$ Nanoparticles. The synthesized core/shell nanoparticles are only dispersible in organic phase as they are coated by long-chain oleate ligands. To enable them for bioapplications, a prerequisite is to make them dispersible in water and in saline buffers. Here, a functional phospholipid polyethylene glycol: 1,2-distearoyl-*sn*-glycero-3-phosphoethanolamine-*N*-[amino(polyethylene glycol)-2000] (ammonium salt) (DSPE-mPEG-2000) was utilized to surface modify the upconverting nanoparticles. Phospholipids mimic cellular membranes to provide a water-dispersible biocompatible surface. The hydrophobic tails of the phospholipid are embedded with the oleate capping ligand of the nanoparticle, consequently exposing a hydrophilic PEGylated surface. Furthermore, the PEG coating can allow prolonged circulation of UCNPs in the bloodstream due to its well-known ability to prevent capture of NPs by the reticuloendothelial system.[37−40] The size of these DSPE-mPEG-2000 coated core/shell UCNPs was measured to be 27.18 ± 1.26 nm from the TEM images (Supporting Information, Figure S10); their hydrodynamic size was evaluated to be ∼61 nm (Supporting Information, Figure S11). Moreover, the stability of DSPE-mPEG-2000 coated core/shell UCNPs in a culture media with 10% fetal bovine serum (FBS) was evaluated by the dynamic light scattering experiment; no aggregations was observed over 7 days, confirming the good colloidal stability of these particles (Supporting Information, Figure S11). A low toxicity of surface modified lanthanide upconverting nanoparticles is important for bioimaging. Various cell viability assays in combination with a broad range of cell lines have shown that UCNPs with good surface treatment are nontoxic within a certain range of concentrations over a defined incubation time.[41] UCNPs-treated *Caenorhabditis elegans* have been shown to thrive at UCNPs concentrations lower than 0.5 mg/mL.[42−44] Evaluation of in vivo toxicity of PEG modified UCNPs in male and female mice have shown 100% survival rate 30 days after injection, with no weight loss.[45,46] To evaluate the toxicity of PEGylated core−shell UCNPs in this study, we performed a typical MTS ((3-(4,5-dimethylthiazol-2-yl)-5-(3-carboxymethoxyphenyl)-2-(4-sulfophenyl)-2H-tetrazolium, sodium salts)) cell viability assay experiment. The result indicated no cytotoxicity at a dose as high as 1 mg/mL over a period of 72 h (Supporting Information, Figure S12).

To examine the suitability of the DSPE-mPEG-2000 coated core/shell nanoparticles for in vivo imaging, we injected a nude mouse via tail vein with the DSPE-mPEG-2000 coated core/shell nanoparticles dispersed in PBS at a dose of ∼2 mg/kg). The nude mouse was imaged for in vivo PL at 1 h postinjection using the Maestro fluorescence imaging system (CRi). Subsequently, the nude mouse was sacrificed, and major organs were taken out for imaging. The core/shell nanoparticles were excited at 980 nm by a fiber-coupled laser diode introduced into the imaging chamber; the laser beam was diverging from the fiber end. The scattered excitation light was cut off by an emission filter (850 SP, Andover) in front of the imaging camera objective.[13,47] Figure 9 displays the whole-animal imaging results of a nude mouse. Figure 9 a, c, e shows bright field images of the intact mouse from the belly, opened mouse from the belly, and extracted main organs, respectively. Figure 9 b, d, f shows the corresponding merged UC PL images of Figure a, c, e, respectively. As shown in Figure 9, high contrast

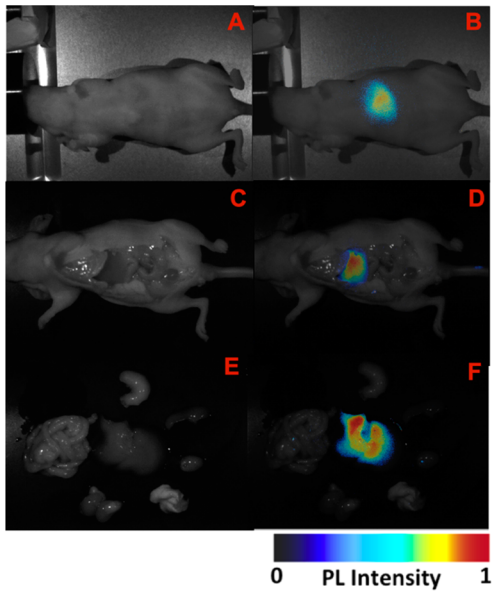

Figure 9. Whole-body imaging of a nude mouse injected via tail vein with the DSPE-mPEG-2000 coated (β-$NaYbF_4$:Gd^{3+} 30%, Tm^{3+} 0.5%) @$NaYF_4$ core−shell nanoparticles. (a, c, e) bright-field images; (b, d, f) corresponding merged bright-field and UC PL images of (a, c, e). The (a, b) images were taken at the belly position in the live mouse, while the (c, d) images were taken at the belly position after the mouse was sacrificed. The (e, f) images were from the extracted internal organs from the sacrificed mouse. The UC PL imaging is displayed in an intensity-coded mode.

UC PL images are obtained under different imaging conditions using the Maestro imaging system. Moreover, DSPE-mPEG-2000 coated core/shell UCNPs exhibited mainly uptake by the liver, with no detectable UC PL in other major organs (Figure 9 e and f). This is in good agreement with previous results on PEG-*b*-PAAc modified UCNPs which were only accumulated in liver, in marked contrast to the result on unmodified UCNPs that were uptake by most organs (lung, liver, spleen, kidney and lymph node).[48] This consistence confirmed the importance of PEGylation on UCNPs for bioimaging. Moreover, the uptake of DSPE-mPEG-2000 coated core/shell UCNPs by the liver most probably arise from their large hydrodynamic size of ∼61 nm, which falls within the size range of 50−250 nm that is known to be effectively absorbed by liver and/or spleen through reticuloendothelial system (RES).[49]

CONCLUSION

In summary, we have systematically investigated the preparation, phase and size control, emission enhancement, and bioimaging applications of Tm^{3+}-doped $NaYbF_4$ NIR-to-NIR UCNPs. It has been shown that doping varied concentrations of Gd^{3+} can convert $NaYbF_4$:Tm^{3+} 0.5% nanoparticles with cubic phase and irregular shape, into highly monodisperse $NaYbF_4$:Tm^{3+} 0.5% nanoplates or nanospheres in a pure hexagonal-phase and of varying size. Moreover, the intensity and the lifetime of NIR UC PL at 800 nm showed a direct dependence on the average size of the resulting nanoparticles, being accredited to the varied corresponding surface-to-volume ratios. An epitaxial growth of a thin $NaYF_4$ shell layer of ∼2 nm on the ∼22 nm core of hexagonal $NaYbF_4$:Gd^{3+} 30%/Tm^{3+} 0.5% nanoparticles can effectively suppress surface-related quenching mechanisms, leading the NIR UC PL of the core nanoparticles to be enhanced by 350 folds. High contrast in

vivo NIR-to-NIR imaging of a nude mouse has been demonstrated using a dispersion of phospholipid-polyethylene glycol (DSPE-PEG)-coated hexagonal core/shell ($NaYbF_4$:Gd^{3+} 30%/Tm^{3+} 0.5%)/$NaYF_4$ nanoparticles in phosphate buffered saline, illustrating the suitability of Tm^{3+}-doped hexagonal $NaYbF_4$ UCNPs for use as imaging contrast agents.

EXPERIMENTAL SECTION

Synthesis of $NaYb_{(1-x)}Gd_{(x)}F_4$: Tm^{3+} 0.5% Core Nanoparticles. All materials used in the experiment were purchased from Sigma-Aldrich and used as received. The synthesis of Tm^{3+}-doped $NaYb_{(1-x)}Gd_xF_4$ nanoparticles (x = 0%, 20%, 30%, 40%, 50%, 70%) was done by growing the nuclei at low temperature via ion diffusion, with subsequent Ostwald-Ripening at higher temperature.[50] The combined amount of $GdCl_3{\cdot}6H_2O$ and $YbCl_3{\cdot}6H_2O$ used for each kind of nanoparticles was set to 1 mmol in total, while $TmCl_3{\cdot}6H_2O$ was maintained constant at 0.5% mmol. Appropriate amounts of $GdCl_3{\cdot}6H_2O$, $YbCl_3{\cdot}6H_2O$, and $TmCl_3{\cdot}6H_2O$ were dissolved in 1 mL of distilled H_2O in a 100 mL three-necked flask prior to addition of 15 mL of oleic acid (90%, technical grade) and 23 mL of 1-octadecene (70%, technical grade). The mixture was heated to 160 °C and maintained for 1 h under Ar gas, with constant stirring to remove H_2O and O_2. The solution was then cooled to 50 °C, before slowly adding 10 mL of solution of methanol containing 4 mmol NH_4F and 2.5 mmol NaOH. After it was stirred for 30 min, methanol was evaporated at 80 °C, the temperature was subsequently increased to 300 °C and maintained for 1.5 h under Ar gas protection. The final solution was cooled to room temperature; the resulting nanoparticles were collected by adding an excess amount of acetone and then centrifuged at 11000 rpm for 10 min. The precipitate was washed with a 1:1 mixture of ethanol/H_2O and finally dispersed in 10 mL of hexane for further uses.

Synthesis of $NaYb_{70}Gd_{30}F_4$: Tm^{3+} 0.5%@$NaYF_4$ Core–Shell Nanoparticles. The shell precursor was prepared by mixing 0.5 mmol of Y_2O_3 with 10 mL of 50% trifluoroacetic acid in a 100 mL three-necked flask and then refluxed at 95 °C until completely dissolved. One mmol $Y(CF_3COO)_3$ precursor was obtained by evaporating the clear solution to dryness under Ar purge. Sodium trifluoroacetate (2.0 mmol) and the $NaYbF_4$:Gd^{3+} 30%, Tm^{3+} 0.5% core in hexane (1.0 mmol) were then added together with 10 mL of oleic acid and 12 mL of octadecene. The mixture was then degassed at 120 °C for 30 min under Ar to remove the remaining water and oxygen. The resulting solution was then heated to 320 °C (~15 °C/min) and kept at this temperature for 30 min before naturally cooling down to room temperature. Addition of 10 mL ethanol to precipitate the nanopaticles was done followed by centrifugation at 9 000 rpm for 7 min. The collected precipitate is dispersed in 10 mL of hexane for further uses.

Water-Dispersible $NaYb_{70}Gd_{30}F_4$: Tm^{3+} 0.5%@$NaYF_4$ Core–Shell Nanoparticles by Phospholipid Micelle Encapsulation. Prior to encapsulation, the hexane solvent was evaporated and the core–shell nanoparticles were redispersed in chloroform at a final concentration of 1 mg/mL. To encapsulate the particles, a chloroform solution of DSPE-mPEG-2000 phospholipid (1,2-distearoyl-*sn*-glycero-3-phosphoethanolamine-N-[methoxy(polyethylene glycol)-2000] (ammonium salt), Avanti) was mixed with the nanoparticles at a 1:4 (UCNP:DSPE-mPEG-2000) weight ratio in a 1 dram vial and was left overnight under the hood to evaporate chloroform. To ensure complete solvent removal, a rotary evaporator was used with a water bath at 60 °C for 30 min. The resulting film was then hydrated with 1 mL of H_2O and filtered through a 0.2 μm syringe filter. The solution was then centrifuged at 13000 rpm for 15 min and the collected particles were redispersed in PBS solution and stored at 4 °C for future use.

Characterization. The size and the morphology of the resulting nanoparticles were characterized by transmission electron microscopy (TEM) using a JEM-2010 microscope at an acceleration voltage of 200 kV. The powder X-ray diffraction (XRD) patterns were recorded by a Siemens D500 diffractometer, using Cu Kα radiation (λ = 0.15418 nm). The 2θ angle of the XRD spectra was recorded at a scanning rate of 5°/min. UC PL spectra were recorded using a Fluorolog-3.11 Jobin Yvon spectrofluorometer, with a slit width defining a spectral resolution of 1 nm. The PL was excited at 975 nm using a fiber-coupled laser diode (Q-Photonics). All UC PL spectra have been corrected for the spectral sensitivity of the system. The PL decay profiles at 800 nm were recorded with an Infinium oscilloscope (Hewlett-Packard) coupled to the PMT of the Fluorolog-3.11 Jobin Yvon spectrofluorometer. A laser diode from Q-Photonics operating at 975 nm was used as the excitation source. When measuring PL decays, the laser diode was operated in a pulsed mode with a repetition of 400 Hz and a pulse width of 80 μs. Dynamic light scattering was performed by a 90Plus zeta sizer (Brookhaven Inc., NY) to monitor the hydrodynamic diameter of the resulting DSPE-mPEG-2000 coated core/shell nanoparticles. They were dispersed in Minimum Essential Medium-alpha (Gibco) containing 10% fetal bovine serum maintaining a 1 mg/mL concentration.

In Vitro Cytotoxicity Assay. HeLa cells were dispensed into a 96-well flat-bottom microplate (Nunc) (~10000 cells/well) using MEM-alpha medium with 10% FBS, and allowed to attach to the bottom of the microplate overnight. Cell viability was assessed by the CellTiter 96 AQueous One Solution Cell Proliferation Assay. Hela cells were treated with different concentrations of PEGylated core/shell UCNPs for 12, 24, and 72 h. After the treatment, cellular media was changed to remove UCNPs, and the AQueous One Solution was added to the cells. Subsequently, the HeLa cells were incubated for 4 h inside an incubator (37 °C, 5.5% CO_2). Lastly, absorbance was measured at 490 nm using a microplate reader (Bio-Tek Synergy HT microplate reader). Tests were performed in 4 replicates.

In Vivo Imaging. NIR fluorescent imaging of BALB/c mouse was performed using a wavelength-resolved Maestro in vivo optical imaging system (CRI, Inc., US) operating at a cube acquisition mode. The phospholipid encapsulated core@shell ($NaYbF_4$:Gd^{3+} 30%, Tm^{3+} 0.5%)@$NaYF_4$ nanoparticles in PBS solution were administered intravenously via the tail vein injection at a dose of ~2 mg/kg. When acquiring wavelength-resolved imaging cubes, the tunable filter was automatically stepped in 10 nm increments from 580 to 950 nm, while the camera captured images at each wavelength with a constant exposure. The overall acquisition time was about 10 s. The autofluorescence spectra and the spectra from the core@shell ($NaYbF_4$:Gd^{3+} 30%, Tm^{3+} 0.5%)@$NaYF_4$ nanoparticles were manually selected from spectral image using the computer mouse to choose appropriate regions. Spectral unmixing algorithms (available from CRi) were applied to create the unmixed images of autofluorescence and the UC PL signal. When appropriately generated, the autofluorescence image should be uniform in intensity, regardless of the presence or absence of the UC PL. The resulting UC PL images are displayed in an intensity-coded mode.

ASSOCIATED CONTENT

Supporting Information

XRD and TEM images for Gd^{3+} 5% and Gd^{3+} 7%, histogram of nanocrystal size distribution, summary of average diameter and standard deviation; plot of the inverse of lifetime of $^3H_4$ state as a function of surface/volume ratio, decay profiles for NIR PL at 800 nm of the $NaYbF_4$:Gd^{3+} 30%, Tm^{3+} 0.5% core and ($NaYbF_4$:Gd^{3+} 30%, Tm^{3+} 0.5%)@$NaYF_4$ core–shell; comparison of the PL spectra of ~100 nm nanoparticles $NaYbF_4$:Gd^{3+} 10%, Tm^{3+} 0.5% and the ~25 nm core–shell ($NaYbF_4$:Gd^{3+} 30%, Tm^{3+} 0.5%)@$NaYF_4$ nanoparticles; TEM image and the size distribution of the DSPE-mPEG-2000 coated core/shell ($NaYbF_4$:Gd^{3+} 30%,Tm^{3+} 0.5%)@$NaYF_4$ UCNPs. This material is available free of charge via the Internet at http://pubs.acs.org

AUTHOR INFORMATION

Corresponding Authors

*E-mail: guanying@buffalo.edu.

*E-mail: pnprasad@buffalo.edu.

Notes

The authors declare no competing financial interest.

■ ACKNOWLEDGMENTS

This work was supported by grants from the National Institutes of Health (R01CA119358 and RO1CA104492), the Swedish Energy Agency (project 32076-1), Natural Science Foundation of China (51102066), Program for Basic Research Excellent Talents in Harbin Institute of Technology (BRETIII 2012018), Fundamental Research Funds for the Central Universities (Harbin Institute of Technology), and the John R. Oishei Foundation. We thank Dr. Wing-Cheung Law, Mr. Xianliang Wang, and Ms. Victoria Vasso for their useful discussions, as well as Dr. Lisa A Eagler for her help on HeLa cells for MTS assay.

■ ABBREVIATIONS

UCNPs, upconversion nanoparticles
NIR, near-infrared
PL, photoluminescence
HRTEM, high resolution transmission electron microscope
DSPE-mPEG-2000, polyethylene glycol 1,2-distearoyl-*sn*-glycero-3-phosphoethanolamine-*N*-[amino(polyethylene glycol)-2000] (ammonium salt)

■ REFERENCES

(1) Prasad, P. N. *Introduction to Nanomedicine and Nanobioengineering*; Wiley: Hoboken, NJ, 2012.
(2) König, K. Multiphoton Microscopy in Life Sciences. *J. Microsc.*. **2000**, *200* (2), 83−104.
(3) Prasad, P. N. *Introduction to Biophotonics*; Wiley: Hoboken, NJ, 2003.
(4) Frangioni, J. In Vivo Near-Infrared Fluorescence Imaging. *Curr. Opin. Chem. Biol.* **2003**, *7*, 626−634.
(5) Hilderbrand, S.; Weissleder, R. Near-Infrared Fluorescence: Application to In Vivo Molecular Imaging. *Curr. Opin. Chem. Biol.* **2010**, *14*, 71−79.
(6) Chatterjee, D.; Rufaihah, A.; Zhang, Y. Upconversion Fluorescence Imaging of Cells and Small Animals Using Lanthanide Doped Nanocrystals. *Biomaterials* **2008**, *29*, 937−943.
(7) Bünzli, J.-C. G. Lanthanide Luminescence for Biomedical Analyses and Imaging. *Chem. Rev.* **2010**, *110*, 2729−2755.
(8) Wang, F.; Banerjee, D.; Liu, Y.; Chen, X.; Liu, X. Upconversion Nanoparticles in Biological Labeling, Imaging, and Therapy. *Analyst* **2010**, *135*, 1839−1854.
(9) Zhou, J.; Liu, Z.; Li, F. Upconversion Nanophosphors for Small-Animal Imaging. *Chem. Soc. Rev.* **2012**, *41*, 1323−1349.
(10) Auzel, F. Upconversion and Anti-Stokes Processes with f and d ions in Solids. *Chem. Rev.* **2004**, *104*, 139−173.
(11) Wu, S.; Han, G.; Milliron, D.; Aloni, S.; Altoe, V.; Talapin, D.; Cohen, B.; Schuck, P. Non-Blinking and Photostable Upconverted Luminescence from Single Lanthanide-Doped Nanocrystals. *Proc. Natl. Acad. Sci. U.S.A.* **2009**, *106*, 10917−10921.
(12) Chen, G.; Ohulchanskyy, T.; Kumar, R.; Agren, H.; Prasad, P. Ultrasmall Monodisperse $NaYF_4$:Yb^{3+}/Tm^{3+} Nanocrystals with Enhanced Near-Infrared to Near-Infrared Upconversion Photoluminescence. *ACS Nano* **2010**, *4*, 3163−3168.
(13) Chen, G.; Shen, J.; Ohulchanskyy, T.; Patel, N.; Kutikov, A.; Li, Z.; Song, J.; Pandey, R.; Agren, H.; Prasad, P.; Han, G. (α-NaYbF4:Tm^{3+})/CaF_2 Core/Shell Nanoparticles with Efficient Near-Infrared to Near-Infrared Upconversion for High-Contrast Deep Tissue Bioimaging. *ACS Nano* **2012**, *6*, 8280−8287.
(14) Prorok, K.; Bednarkiewicz, A.; Cichy, B.; Gnach, A.; Misiak, M.; Sobczyk, M.; Strek, W. The Impact of Shell Host ($NaYF_4$/CaF_2) and Shell Deposition Methods on the Up-conversion Enhancement in Tb^{3+}, Yb^{3+} Codoped Colloidal α–$NaYF_4$ Core-Shell Nanoparticles. *Nanoscale* **2014**, *6*, 1855−1864.
(15) Krämer, K. W.; Biner, D.; Frei, G.; Güdel, H. U.; Hehlen, M. P.; Lüthi, S. R. Hexagonal Sodium Yttrium Fluoride Based Green and Blue Emitting Upconversion Phosphors. *Chem. Mater.* **2004**, *16*, 1244−1251.
(16) Niu, N.; He, F.; Gai, S.; Li, C.; Zhang, X.; Huang, S.; Yang, P. Rapid Microwave Reflux Process for the Synthesis of Pure Hexagonal $NaYF_4$:Yb^{3+},Ln^{3+},Bi^{3+} (Ln^{3+} = Er^{3+}, Tm^{3+}, Ho^{3+}) and Its Enhanced UC Luminescence. *J. Mater. Chem.* **2012**, *22*, 21613−21623.
(17) Ehlert, O.; Thomann, R.; Darbandi, M.; Nann, T. A Four-Color Colloidal Multiplexing Nanoparticle System. *ACS Nano* **2008**, *2*, 120−124.
(18) Chen, G.; Ohulchanskyy, T. Y.; Law, W. C.; Agren, H.; Prasad, P. N. Monodisperse $NaYbF_4$:Tm^{3+}/$NaGdF_4$ Core/Shell Nanocrystals with Near-Infrared to Near-Infrared Upconversion Photoluminescence and Magnetic Resonance Properties. *Nanoscale* **2011**, *3*, 2003−2008.
(19) Xing, H.; Bu, W.; Ren, Q.; Zheng, X.; Li, M.; Zhang, S.; Qu, H.; Wang, Z.; Hua, Y.; Zhao, K.; Zhou, L.; Peng, W.; Shi, J. A $NaYbF_4$:Tm^{3+} Nanoprobe for CT and NIR-to-NIR Fluorescent Bimodal Imaging. *Biomaterials* **2012**, *33*, 5384−5393.
(20) Zhan, Q.; Qian, J.; Liang, H.; Somesfalean, G.; Wang, D.; He, S.; Zhang, Z.; Andersson-Engels, S. Using 915 nm Laser Excited Tm^{3+}/Er^{3+}/Ho^{3+}-Doped NaYbF4 Upconversion Nanoparticles for in Vitro and Deeper in Vivo Bioimaging without Overheating Irradiation. *ACS Nano* **2011**, *5*, 3744−3757.
(21) Mai, H.-X.; Zhang, Y.-W.; Si, R.; Yan, Z.-G.; Sun, L.-d.; You, L.-P.; Yan, C.-H. High-Quality Sodium Rare-Earth Fluoride Nanocrystals: Controlled Synthesis and Optical Properties. *J. Am. Chem. Soc.* **2006**, *128*, 6426−6436.
(22) Zeng, S.; Ren, G.; Xu, C.; Yang, Q. Modifying Crystal Phase, Shape, Size, Optical and Magnetic Properties of Monodispersed Multifunctional $NaYbF_4$ Nanocrystals through Lanthanide Doping. *CrystEngComm* **2011**, *13*, 4276−4281.
(23) Chen, D.; Yu, Y.; Huang, F.; Yang, A.; Wang, Y. Lanthanide Activator Doped $NaYb_{1-x}Gd_xF_4$ Nanocrystals with Tunable Down-, Up-conversion Luminescence and Paramagnetic Properties. *J. Mater. Chem.* **2011**, *21*, 6186−6192.
(24) Pan, L.; He, M.; Ma, J.; Tang, W.; Gao, G.; He, R.; Su, H.; Cui, D. Phase and Size Controllable Synthesis of $NaYbF_4$ Nanocrystals in Oleic Acid/Ionic Liquid Two-Phase System for Targeted Fluorescent Imaging of Gastric Cancer. *Theranostics* **2013**, *3*, 210−222.
(25) Chen, D.; Wang, Y. Impurity Doping: A Novel Strategy for Controllable Synthesis of Functional Lanthanide Nanomaterials. *Nanoscale* **2013**, *5*, 4621−4637.
(26) Chen, D.; Yu, Y.; Huang, F.; Huang, P.; Yang, A.; Wang, Y. Modifying the Size and Shape of Monodisperse Bifunctional Alkaline-Earth Fluoride Nanocrystals through Lanthanide Doping. *J. Am. Chem. Soc.* **2010**, *132*, 9976−9978.
(27) Qiu, H.; Chen, G.; Fan, R.; Cheng, C.; Hao, S.; Chen, D.; Yang, C. Tuning the Size and Shape of Colloidal Cerium Oxide Nanocrystals through Lanthanide Doping. *Chem. Commun.* **2011**, *47*, 9648−9650.
(28) Thoma, R. E.; Insley, H.; Hebert, G. M. The Sodium Fluoride−Lanthanide Trifluoride Systems. *Inorg. Chem.* **1966**, *5*, 1222−1229.
(29) Liang, X.; Wang, X.; Zhuang, J.; Peng, Q.; Li, Y. Synthesis of $NaYF_4$ Nanocrystals with Predictable Phase and Shape. *Adv. Funct. Mater.* **2007**, *17*, 2757−2765.
(30) Wang, F.; Han, Y.; Lim, C.; Lu, Y.; Wang, J.; Xu, J.; Chen, H.; Zhang, C.; Hong, M.; Liu, X. Simultaneous Phase and Size Control of Upconversion Nanocrystals through Lanthanide Doping. *Nature* **2010**, *463*, 1061−1065.
(31) Shannon, R. Revised Effective Ionic Radii and Systematic Studies of Interatomic Distances in Halides and Chalcogenides. *Acta Crystallogr., Sect. A* **1976**, *32*, 751−767.
(32) Heer, S.; Kömpe, K.; Güdel, H. U.; Haase, M. Highly Efficient Multicolour Upconversion Emission in Transparent Colloids of Lanthanide-Doped $NaYF_4$ Nanocrystals. *Adv. Mater.* **2004**, *16*, 2102−2105.

(33) Karl, W. K.; Daniel, B.; Gabriela, F.; Hans, U. G.; Markus, P. H.; Stefan, R. L. Hexagonal Sodium Yttrium Fluoride Based Green and Blue Emitting Upconversion Phosphors. *Chem. Mater.* **2004**, *16*, 1224−1251.
(34) Jingning, S.; Mruthunjaya, U.; Nan, Y.; Yiguang, J. Anomalous Raman Scattering of Colloidal Yb^{3+},Er^{3+} Codoped $NaYF_4$ Nanophosphors and Dynamic Probing of the Upconversion Luminescence. *Adv. Funct. Mater.* **2010**, *20*, 3530−3537.
(35) Chen, G.; Yang, C.; Prasad, P. Nanophotonics and Nanochemistry: Controlling the Excitation Dynamics for Frequency Up- and Down-Conversion in Lanthanide-Doped Nanoparticles. *Acc. Chem. Res.* **2013**, *46*, 1474−1486.
(36) Chen, G.; Qiu, H.; Prasad, P. N.; Chen, X. Upconversion Nanoparticles: Design, Nanochemistry, and Applications in Theranostics. *Chem. Rev.* **2014**, *114*, 5161−5214.
(37) Liu, Z.; Davis, C.; Cai, W.; He, L.; Chen, X.; Dai, H. Circulation and Long-Term Fate of Functionalized, Biocompatible Single-Walled Carbon Nanotubes in Mice Probed by Raman Spectroscopy. *Proc. Natl. Acad. Sci. U. S. A.* **2008**, *105*, 1410−1415.
(38) Knop, K.; Hoogenboom, R.; Fischer, D.; Schubert, U. Poly(Ethylene Glycol) in Drug Delivery: Pros and Cons as well as Potential Alternatives. *Angew. Chem., Int. Ed.* **2010**, *49*, 6288−6308.
(39) Fang, J.; Nakamura, H.; Maeda, H. The EPR effect: Unique Features of Tumor Blood Vessels for Drug Delivery, Factors Involved, and Limitations and Augmentation of the Effect. *Adv. Drug Delivery Rev.* **2011**, *63*, 136−151.
(40) Jokerst, J. V.; Lobovkina, T.; Zare, R. N.; Gambhir, S. S. Nanoparticle PEGylation for Imaging and Therapy. *Nanomedicine* **2011**, *6*, 715−728.
(41) Gu, Z.; Yan, L.; Tian, G.; Li, S.; Chai, Z.; Zhao, Y. Recent Advances in Design and Fabrication of Upconversion Nanoparticles and Their Safe Theranostic Applications. *Adv. Mater.* **2013**, *25*, 3758−3759.
(42) Lim, S.; Riehn, R.; Ryu, W. S.; Khanarian, N.; Tung, C.-k.; Tank, D.; Austin, R. H. In Vivo and Scanning Electron Microscopy Imaging of Upconverting Nanophosphors in *Caenorhabditis elegans*. *Nano Lett.* **2006**, *6*, 169−174.
(43) Zhou, J.; Yang, Z.; Dong, W.; Tang, R.; Sun, L.; Yan, C. Bioimaging and Toxicity Assessments of NearInfrared Upconversion Luminescent $NaYF_4$:Yb,Tm Nanocrystals. *Biomaterials* **2011**, *32*, 9059−9067.
(44) Chen, J.; Guo, C.; Wang, M.; Huang, L.; Wang, L.; Mi, C.; Li, J.; Fang, X.; Mao, C.; Xu, S. Controllable Synthesis of $NaYF_4$: Yb, Er Upconversion Nanophosphors and Their Application to In Vivo Imaging of Caenorhabditis Elegans. *J. Mater. Chem.* **2011**, *21*, 2632−2638.
(45) Tian, G.; Gu, Z.; Zhao, L.; Yin, W.; Liu, X.; Yan, L.; Jin, S.; Ren, W.; Xing, G.; Li, S.; Zhao, Y. Mn^{2+} Dopant-Controlled Synthesis of $NaYF_4$:Yb/Er Upconversion Nanoparticles for in vivo Imaging and Drug Delivery. *Adv. Mater.* **2012**, *24*, 1226−1231.
(46) Zhou, L.; Gu, Z.; Liu, X.; Yin, W.; Tian, G.; Yan, L.; Jin, S.; Ren, W.; Xing, G.; Li, W.; Chang, X.; Hu, Z.; Zhao, Y. Size-Tunable Synthesis of Lanthanide-Doped Gd_2O_3 Nanoparticles and Their Applications for Optical and Magnetic Resonance Imaging. *J. Mater. Chem.* **2012**, *22*, 966−974.
(47) Nyk, M.; Kumar, R.; Ohulchanskyy, T.; Bergey, E.; Prasad, P. High Contrast In Vitro and In Vivo Photoluminescence Bioimaging Using Near Infrared to Near Infrared Up-Conversion in Tm^{3+} and Yb^{3+} Doped Fluoride Nanophosphors. *Nano Lett.* **2008**, *8*, 3834−3838.
(48) Venkatachalam, N.; Yamano, T.; Hemmer, E.; Hyodo, H.; Kishimoto, H.; Soga, K. Er^{3+}-Doped Y_2O_3 Nanophosphors for Near Infrared Fluorescence Bioimaging Applications. *J. Am. Ceram. Soc.* **2013**, *96*, 2759−2765.
(49) Hemmer, E.; Yamano, T.; Kishimoto, H.; Venkatachalam, N.; Hyodo, H.; Soga, K. Cytotoxic Aspects of Gadolinium Oxide Nanostructures for Up-Conversion and NIR Bioimaging. *Acta Biomater.* **2013**, *9*, 4734−4743.
(50) Li, Z.; Zhang, Y. An Efficient and User-Friendly Method for the Synthesis of Hexagonal-Phase $NaYF_4$:Yb, Er/Tm Nanocrystals with Controllable Shape and Upconversion Fluorescence. *Nanotechnology* **2008**, *19*, No. 345606.